Journal of Alloys and Compounds 1040 (2025) 183282

Contents lists available at ScienceDirect

Journal of Alloys and Compounds

journal homepage: www.elsevier.com/locate/jalcom

Research article

Non-equilibrium phase regime and magnetic properties of co-evaporated Fe-V thin-films

Simon Rauls [a,*], Benedikt Eggert [a], Shadab Md. Anwar [b], Tobias Lojewski [a], Tom Helbig [a], Aleksandr Chumakov [c], Dimitrios Bessas [c], Radu Abrudan [d], Katharina Ollefs [a], Kay Potzger [b], Jürgen Fassbender [b,e], Rantej Bali [b], Heiko Wende [a]

[a] Faculty of Physics and Center for Nanointegration Duisburg–Essen (CENIDE), University of Duisburg–Essen, Lotharstr. 1, Duisburg, 47057, Germany
[b] Institute of Ion Beam Physics and Materials Research, Helmholtz-Zentrum Dresden - Rossendorf, Bautzner Landstraße 400, Dresden, 01069, Germany
[c] ESRF-The European Synchrotron, CS 40220, Grenoble Cedex 9, 38043, France
[d] Helmholtz-Zentrum Berlin für Materialien und Energie, Hahn-Meitner-Platz 1, Berlin, 14109, Germany
[e] Institute of Solid State and Materials Physics, Dresden University of Technology, Haeckelstraße 3, Dresden, 01069, Germany

ARTICLE INFO

Keywords:
FeV alloy
Iron-vanadium alloy
Thin-films
Short-range order
Mössbauer spectroscopy
XMCD
Vibrational density of states VDOS
Magnetometry
Nuclear inelastic scattering NIS/NRIXS

ABSTRACT

At equiatomic composition, FeV alloys form metastable phases such as the B2 phase or a short-range ordered phase in favor of the equilibrium σ phase. In this regime, structural, magnetic, and vibrational properties are strongly influenced by atomic disorder. For thermally co-evaporated $Fe_{1-x}V_x$ thin-films, the non-equilibrium phase diagram is explored and the short-range ordered phase that forms at equiatomic compositions is compared to its base-centered cubic counterpart. The results indicate that within the short-range ordered thin-films, the structural disorder is accompanied by an increase in chemical order, i.e. Fe and V atoms are their respective preferential nearest neighbors. These observations are important for a better understanding of recrystallization in nonmagnetic, short-range ordered templates, in which crystallization can be selectively triggered.

1. Introduction

In intermetallic alloys such as Fe–Al and Fe–Rh, order–disorder transitions can be selectively triggered through laser [1,2] or ion irradiation [3–11], which comes with large variations of their physical properties. In Fe–Al and Fe–Rh for instance, the nonmagnetic, chemically ordered phase can be transformed to a ferromagnetic, chemically disordered phase. In Fe-V [12–14], a transformation from a nonmagnetic, structurally disordered (short-range ordered (SRO)) phase to a ferromagnetic structurally ordered phase can be selectively triggered. Furthermore, in the same composition range, it is possible to address a transition from chemical disorder to chemical order through thermal annealing [15–17], which shows an unusual increase in vibrational entropy upon ordering. Hence, in $Fe_{1-x}V_x$, both structural and chemical disorder need to be considered in understanding the complex interplay between structure, magnetism and vibrational properties. Generally, the binary alloy $Fe_{1-x}V_x$ attracted scientific interest for a variety of characteristics. To name a few, the magnetic coupling between interfaces and bulk alloys is fundamentally different [18–20], the base-centered cubic (*bcc*) crystal has completely suppressed magnetic ordering at V-concentrations above $x = 0.7$ [21,22], at low V-concentration it exhibits a very low Gilbert damping parameter and low saturation magnetization [14,23,24,24–28], and around equiatomic concentration, the structurally complex σ phase appears [21,29–35]. As the σ phase has slow formation kinetics, a metastable phase diagram is also found in a similar concentration and temperature range, revealing preferential B2 order [17], accompanied by an anomalous increase in vibrational entropy [16] or short-range order [30,36]. The coexistence of A2 (*bcc*, chemically disordered quasi solid solution), B2 (*bcc*, ordered/layered *bcc*), SRO (structurally disordered) and the σ phases (structurally complex, 30 atoms/unit cell, partial chemical order [29,31]) often complicates the preparation, characterization, and therefore, the understanding of such structures. This has become particularly evident when trying to explain the magnetic [22] and vibrational properties of the $Fe_{1-x}V_x$ system [15]. In this study, co-evaporated $Fe_{1-x}V_x$ thin-films of varying concentration are investigated. The metastable phase diagram phase will be addressed by comparing two series of samples, one with constant substrate temperature (T_G) of 573 K during growth but varying composition and second, samples with constant V

* Corresponding author.
E-mail address: simon.rauls@uni-due.de (S. Rauls).

https://doi.org/10.1016/j.jallcom.2025.183282
Received 22 April 2025; Received in revised form 21 August 2025; Accepted 24 August 2025
Available online 31 August 2025

concentration of $x = 0.4$ but varying T_G. The results obtained will help to improve the understanding and modeling of structurally and chemically disordered alloys, which will be useful for investigations of phase transformations caused by laser- [13] or ion-irradiation [12,14] and studying disorder induced effects on magnetic [23,27] and vibrational properties [15].

2. Experimental details

Sample preparation: Thin films of $Fe_{1-x}V_x$ with a nominal thickness of 40 nm were prepared using a self-built MBE setup under UHV-conditions (base pressure of 10^{-10} mbar, by co-evaporation of Fe (95% ^{57}Fe)) from a thermal evaporator and V from an electron beam evaporator. Before evaporation, the isopropyl-alcohol cleaned Si(001)/270 nm SiO_2 substrates were heated to 573 K for 30 min under UHV conditions and cooled down or heated up towards the specified growth temperature T_G. The combined growth rate of Fe and V was held constant throughout the sample series using 0.18 Å/s. No further annealing steps were performed. The enrichment with ^{57}Fe on the final samples is essential to achieve a high signal-to-noise ratio of the Mössbauer spectra and the Nuclear Inelastic Scattering.

Vibrating sample magnetometry: Vibrating sample magnetometry (VSM) was performed at 300 K in a Quantum Design Dynacool PPMS system, using the VSM option with the magnetic field parallel to the surface plane. Volume-magnetizations were recalculated employing the weight of the sample and assuming 40 nm thickness.

X-ray diffraction: X-ray diffraction (XRD) patterns were recorded using a Phillips PW1730 diffractometer with Cu K_α radiation at a wavelength of 1.54 Å. Samples were aligned in reflectivity using the total external reflection at 0.8°. Fitting was performed, using the software package Pi [37].

Mössbauer spectroscopy: ^{57}Fe Mössbauer spectroscopy at perpendicular incidence of the γ-rays onto the film surface was performed by detection of conversion electrons (CEMS). For the detection of the electrons, the sample was installed in a proportional gas counter, i.e. housing with a continuous He gas flow mixed with 4% CH_4 to avoid ionization processes. For the measurement, a constant acceleration Mössbauer driving unit was used with a ^{57}Co source embedded in a Rh matrix, while the velocity of the spectrometer was calibrated with an α-Fe foil reference sample at room temperature. The experimental spectra were evaluated by a least-squares fitting routine using the Pi software package [37], using the Hesse-Rübartsch method with a smoothing parameter between 0.2 and 1, still allowing for discrete hyperfine field values, especially at low V concentration. Because of the statistical nature of local environments in the sample, the hyperfine field was fixed to depend linearly on the isomer shift in the fashion: $\delta_{iso} = IS + \Delta_{iso} \cdot B_{HF}$

X-ray magnetic circular dichroism: For a range of samples, X-ray magnetic circular dichroism was measured at beamline PM3 at BESSY II in Berlin [38]. To avoid large contributions of native oxide, the samples were grown onto silicon-nitride membranes to allow for measurements in transmission geometry. To achieve this, the sample surface plane was rotated 37° relative to the synchrotron beam, in order to have large enough projected area of the membrane window and high projection of the in-plane magnetization. The magnetic field was parallel to the surface plane to allow for easy switching of the in-plane magnetization. Throughout the measurements, the helicity of the X-rays was fixed and the dichroic signal was obtained by switching the magnetic field orientation.

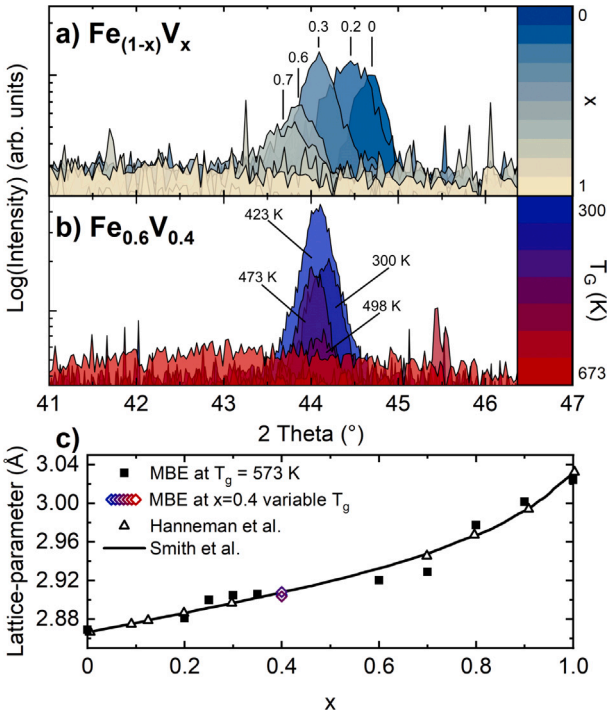

Fig. 1. Concentration dependence (a) of the (110) Bragg reflection of $Fe_{1-x}V_x$ grown at 573 K and growth temperature dependence (b) of $Fe_{0.6}V_{0.4}$. The resulting lattice constants (c) in comparison to literature [40,41] with full squares for T_G = 573 K and open tilted squares with color according to the growth temperature in (b).

Nuclear Inelastic Scattering: Inelastic nuclear scattering measurements were performed at the nuclear resonance beamline (former ID18) at the European Synchrotron Radiation Facility (ESRF) in Grenoble [39] in reflectivity at an incidence angle of 0.288° using an avalanche photodiode mounted closely above the thin-film surface. The spectra were obtained using the high resolution monochromator with an energy resolution of ~0.8 meV (FWHM) at the nuclear resonance of ^{57}Fe at 14.4 keV. Energy calibration was performed using powdered $(NH_4)_2Mg^{57}Fe(CN)_6$.

3. Results

Fig. 1(a) shows the dependence of the position and intensity of the (110) Bragg reflection as a function of x, measured for the $Fe_{1-x}V_x$ alloy thin films grown at 573 K. For the full patterns, please see the supplementary material. With increasing x, the Bragg reflection shifts to smaller angles, indicating larger lattice constants. Furthermore, increasing the V content, the Bragg reflections broaden until the peaks vanish and become almost indistinguishable from the background. In particular, at $x = 0.4$ and 0.5, the Bragg reflection vanishes and recovers at $x = 0.6$ and 0.7, until it vanishes at higher V content. The variation of the (110) Bragg reflection as a function of growth temperature T_G for $x = 0.4$, depicted below in Fig. 1 (b) shows a sharp (110) Bragg reflection only at low growth temperatures, whereas it strongly broadens at higher temperatures. Fig. 1(c) shows the lattice constants obtained by refining with an A2 $Fe_{1-x}V_x$ model. The (100) peaks indicating B2 order were not observed for any of the samples. The results are compared to the results of Hannemann and Smith [40,41] for bulk systems. The progression of the lattice constants exhibits nonlinear behavior, deviating from Vegard's rule for smaller lattice constants.

Fig. 2(a) shows the first quadrant of magnetic hysteresis curves and Fig. 2(b) the corresponding concentration dependent saturation moments for samples grown at 573 K as average moment per atom and as

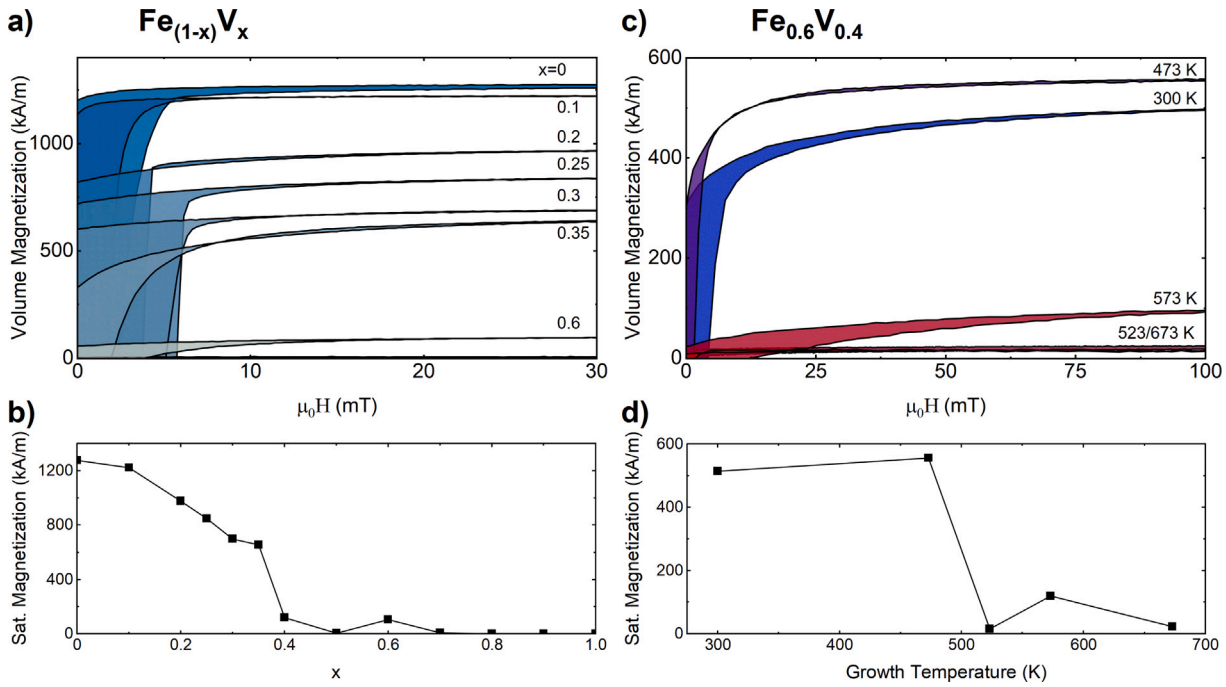

Fig. 2. Volume magnetization and corresponding atomic saturation moment for (a),(b) concentration dependence of $Fe_{1-x}V_x$ grown at 573 K and (c),(d) growth temperature dependence of $Fe_{0.6}V_{0.4}$. At high temperatures and intermediate V concentrations, there is a sudden drop in saturation magnetization, reflecting the change from ferromagnetic *bcc* to paramagnetic/weakly ferromagnetic for the short-range ordered phase. At concentrations above $x = 0.7$ V, the magnetic moment is completely quenched, as is expected for their Pauli-paramagnetic character. Volume magnetization in kA/m translates to the same values in emu/cm^3.

moment per Fe-atom within the sample. The saturation magnetization decreases with increasing V concentration until for $0.4 \leq x < 0.6$ it is strongly reduced to very low values for the short-range ordered thin films. For $x = 0.6$, where the sample is A2 ordered again, a slight increase of M_S is observed which is suppressed for $x = 0.7$ and above. The growth temperature dependence in Fig. 2(c)&(d) shows high saturation magnetization for low growth temperatures, with the sample grown at 473 K slightly surpassing the sample grown at 300 K. At higher temperatures, where the XRD suggests only short-range order, the saturation magnetization vanishes except for $T_G = 573$ K, indicating the presence of magnetic ordering.

The CEMS method is susceptible to hyperfine interactions such as local changes in electron density, electric field gradients or magnetic fields around the ^{57}Fe nuclei within the sample. Fig. 3(a) and (b) shows the CEMS and corresponding mean hyperfine magnetic fields and mean isomer shifts obtained from fitting via the Hesse-Rübartsch method as already explained in Section 2. For pure Fe in Fig. 3(a), a sharp sextet split spectrum is observed, corresponding to ferromagnetic, *bcc* Fe with a hyperfine field splitting of 32.2 T with the hyperfine field oriented in the sample plane, as expected from the large shape anisotropy of the thin film. For $x = 0.1$, the spectrum smears out towards a lower hyperfine field splitting. Upon closer examination, two main hyperfine field contributions become apparent. One possesses a slightly higher hyperfine field than pure Fe, while the other has a slightly lower one. Further increase of x leads to additional broadening and decreasing of the hyperfine fields, until the hyperfine field is completely diminished for $x = 0.4$ and 0.5, and only a single asymmetric resonance is detected for the SRO and paramagnetic/weakly ferromagnetic samples. For $x = 0.6$, a broad hyperfine field distribution is detected again, and a further increase in V content only results in completely diminished hyperfine fields, corresponding to their paramagnetic character. This behavior is represented in Fig. 3(b), depicting the mean hyperfine field and the mean isomer shift. The mean hyperfine field is reduced with increasing x for the *bcc* samples and it vanishes for the SRO samples as well as for the samples with $x \geq 0.7$, which reflects their paramagnetic behavior. In contrast, for the mean isomer shift, a linear functionality of the decrease is observed for the *bcc* ordered samples, whereas a large decrease of the isomer shift is observed for the short-range ordered samples. In Fig. 3(c), the CEMS for $Fe_{0.6}V_{0.4}$ is shown for different growth temperatures T_G. The SRO samples grown at high substrate temperature show a single asymmetric resonance, whereas the samples grown at lower substrate temperature become ferromagnetic and, therefore, show a broad hyperfine sextet.

To verify the occurrence of antiparallel coupling between the Fe and V moments, XMCD was measured on a *bcc* sample at a concentration of $x = 0.4$ (see Fig. 4), illustrating measurements at both the Fe and V $L_{2,3}$ edges. The antiparallel coupling is evident from the different signs of the XMCD for both elements. The antiparallel-induced moments in V have been shown to originate from short-range polarization, a direct result of hybridization with Fe [19,20,42]. By application of XMCD sum rules, a Fe spin moment of 1.12 μ_B and an orbital moment of 0.13 μ_B was determined, summing up to a total magnetic moment of 1.25 μ_B. For V, the orbital moment amounts to −0.11 μ_B, and the spin moment to −0.14 μ_B, summing up to −0.25 μ_B. For Fe, the error can be estimated in the range of 10% and for V, the error might be larger, as its spin-moment might be underestimated by the sum-rules about a factor of 2 due to *jj*-mixing. Please keep in mind that the samples are grown onto a different substrate as explained in Section 2, so this measurement only provides an estimate of the atomic magnetic moments and the indication of antiparallel coupling between Fe and V (see Fig. 4).

Nuclear inelastic scattering has been used to study various types of disordered materials [16,43–47] and was carried out for a concentration of $x = 0.4$ for a SRO sample, grown at 573 K and for a *bcc* (A2) phase, grown at RT. From such measurements, the Fe-partial vibrational density of states (VDOS) can be extracted, allowing for understanding of bond strengths and certain thermodynamic quantities, allowing for interpretations of structural and chemical disorder. While the A2 phase in Fig. 5 shows the expected behavior of the A2 alloy [16], the Fe–partial vibrational density of states (VDOS) of the short-range ordered sample is significantly broadened, and there is a variation in the energy of certain vibrational contributions. As such, the longitudinal acoustic peak at high energies is subject to a stronger broadening

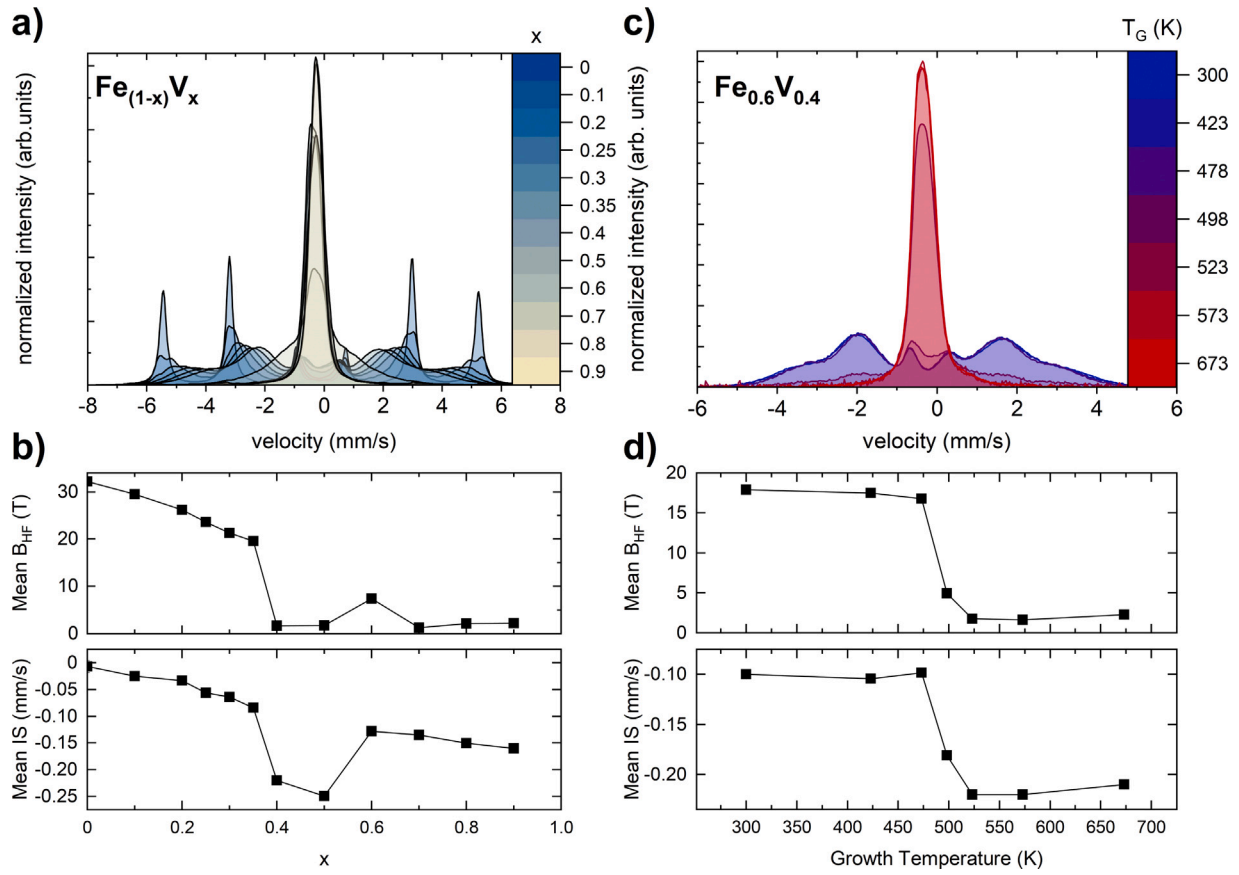

Fig. 3. Area-normalized CEMS spectra and corresponding mean hyperfine fields and mean isomer shifts for (a),(b) concentration dependence of $Fe_{1-x}V_x$ grown at 573 K and (c),(d) growth temperature dependence of $Fe_{0.6}V_{0.4}$. At high growth temperatures and intermediate V concentrations, there is a sudden drop in both hyperfine field and isomer shift, reflecting the change from the ferromagnetic, hyperfine split sextets to the single asymmetric resonance line of the SRO phase and the high V-content alloys.

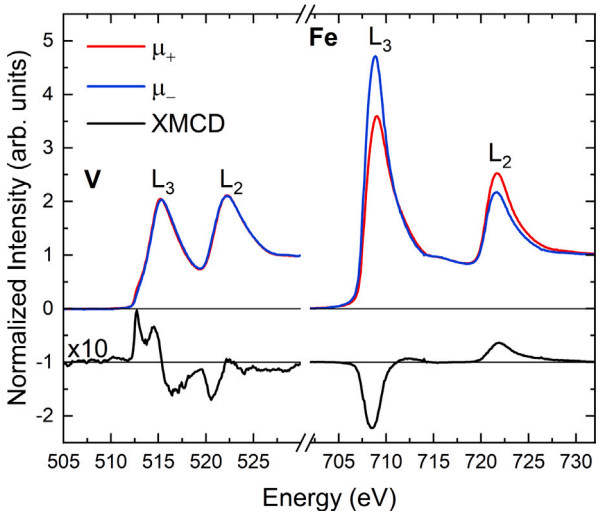

Fig. 4. X-ray absorption spectra (XAS) and XMCD spectra of as-grown polycrystalline $Fe_{0.6}V_{0.4}$. XMCD shifted by −1 for visibility. Measurements were performed at the Fe- and V L3,2 edges in transmission at an angle of 37 degrees with respect to the beam, with a parallel alignment of the magnetic field and the thin-film surface. The antiparallel alignment of Fe and V moments is visible from the different sign of the XMCD at the Fe and V edge.

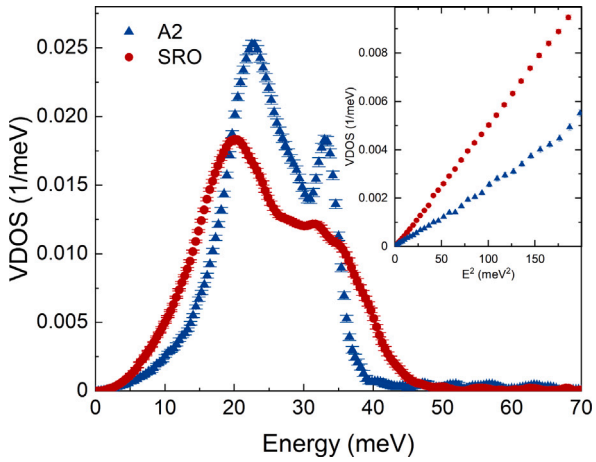

Fig. 5. Fe-partial vibrational density of states derived from measurements of nuclear inelastic scattering for as-grown polycrystalline (A2) and as-grown SRO $Fe_{0.6}V_{0.4}$. Apart from an overall broadening of the VDOS, a softening of the low-energy phonons can be observed for the SRO sample. The inset shows the low-energy region over E^2 in a similar manner to [43].

than the low-energy contributions, but its positional variation is negligible. In comparison, the low-energy contributions show less broadening but a significant softening, i.e. a shift towards lower energies. The inset in Fig. 5 shows the low-energy region of the Fe–partial VDOS over the square of the energy. Both samples show a linear relation corresponding to Debye-like behavior, but the SRO sample shows a larger slope. Upon forming the SRO state, the Fe–partial vibrational

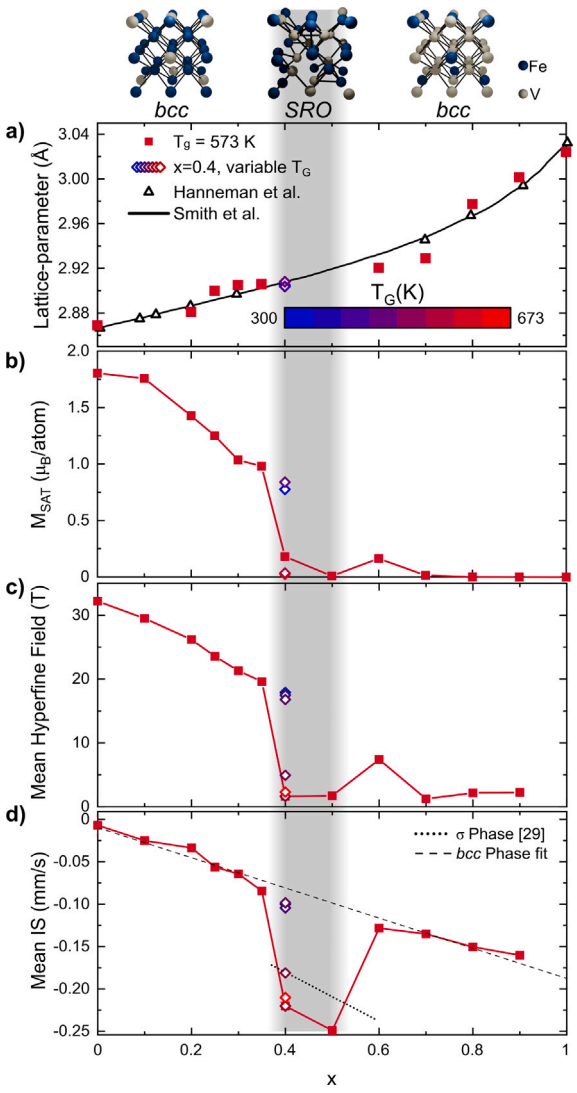

Fig. 6. Concentration dependence of MBE-grown FeV thin-films with varying concentrations (filled squares) and of $Fe_{0.6}V_{0.4}$ with varying temperature (open tilted squares), the shaded area represents the regime of SRO sample growth, also depicted with sketches of the lattice at the top. From top to bottom: Lattice parameter derived from XRD, open triangles and closed line from literature [40,41], as presented in [40]; saturation magnetization from vibrating sample magnetometry; mean hyperfine field of the Mössbauer spectra; mean isomer shift of the Mössbauer spectra relative to α-Fe with IS of −0.107 mm/s.

entropy increases by 0.16(1) k_B/atom, which is higher than what Fultz et al. (0.01(2) k_B/atom) found for *bcc*-Fe compared to nanocrystalline Fe [43], and larger than what Munoz et al. found for A2-B2 $Fe_{0.5}V_{0.5}$ (0.12(3) k_B/atom) [16].

4. Discussion

Preceding the actual discussion of the recent data, some aspects of previous work will be summarized. The SRO Fe–V phase has been reported previously [12,14,30,36]. For magnetron sputtered $Fe_{0.6}V_{0.4}$, it was seen that reordering kinetics under ion-irradiation strongly depend on the short-range structure of the samples, which itself is sensitively dependent on the diffusion kinetics during the sample preparation [14]. As the phase formation of Fe–V occurs at very small length-scales, understanding the atomic arrangements of these SRO thin-films is not trivial, but using EXAFS, different local environments for Fe and V were observed, where the open volume around Fe decreases and the open volume around V increases [12]. The approach of this work to understanding SRO is a combination of examining the reasons behind the SRO phase formation by contrasting structural and magnetic properties of *bcc*-, SRO- and σ-phase and to explore pathways to spectroscopically disentangle chemical and structural ordering phenomena. Fig. 6 summarizes the results obtained from the data presented above. The color coding represents the growth temperature and the shaded area and the sketches of the lattice structure on top represent the concentration regime in which the SRO phase appears. Considering only the *bcc*-phase for now, the XRD 6(a) shows a continuous increase of the lattice constant with increasing x, with shorter lattice constants as expected from Vegard's rule, which usually implies stronger bonds between Fe and V compared to Fe–Fe and V–V. The mean saturation magnetization Fig. 6(b) and the mean hyperfine field Fig. 6(c) both decrease non-linearly upon increasing x, but the saturation magnetization decreases at a faster rate than the mean hyperfine field. To understand this discrepancy, it is necessary to not only take into account the Fe but also the V contributions. As it is known for the FeV system, not only Fe, but also V carries a magnetic moment up to 1 μ_B/atom with antiparallel coupling to the Fe moment which has been found with polarized neutron scattering and XMCD [19,20,42,48–50]. The atomic moments found from XMCD within this study agree that the Fe moment is reduced upon alloying with V, but also V carries an antiparallel moment. The results are in the same order of magnitude as the moments derived from the VSM measurements, with the XMCD total moment slightly overestimating the total moment, which could be due to slight underestimation of the negative V moment due to jj-mixing [51,52] or due to the growth on a different substrate. The most notable difference between the results for the alloy at $x = 0.1$ and $x = 0.15$ (from [20,49,50]) and the measurement at $x = 0.4$ (Fig. 4) is evident in the pre-edge feature of the V L_3 edge, which is more pronounced for $x = 0.4$ in both XAS and XMCD. As a result, it can be noted that with increasing V content, not only does the Fe moment reduce, but also the V moment must be subject to concentration-dependent changes, which is in line with the observations made in [22,48]. The hyperfine fields in Fig. 3 show an overall reduction and a broadening, until the hyperfine fields vanish entirely at $x = 0.7$ and above. For the chemically disordered A2 alloys, this reduction and broadening reflects a distribution of hyperfine fields caused by the statistical probability of different local arrangements of Fe and V 1st, 2nd and 3rd nearest neighbors around the ^{57}Fe absorbers (compare to [22]). For dilute alloys, this means that the hyperfine fields of $Fe_{1-x}V_x$ depend on the binomial probability of the ^{57}Fe nucleus having any number of 1st or 2nd nearest-neighbors replaced by a V atom, which results in a negative modification of the hyperfine field, or a slight enhancement of hyperfine field from the 3rd nearest-neighborhood [22,48,53,54]. Fitting the spectra yields different Δ_{iso} parameters (explained in Section 2) for different concentrations, which indicates varying shifts of the Mössbauer lines depending on the local concentration. This should not be the case, if only the occupation probability of a binomial distribution of local environments changes, and it also cannot be explained by a change of the Fermi contact field. Particularly for non-dilute alloys, this hints at a local environment-dependent magnetic coupling between Fe and V, resulting in a local concentration-dependent shift of the individual hyperfine field contributions. Fig. 6(d) displays the mean central shift of the hyperfine field distribution. For the *bcc*-phase a linear decrease of the isomer shift is observable over the whole concentration range. This reduction of the isomer shift corresponds to a larger electron density at the position of the Fe nucleus, which counteracts the concentration-dependent increase of the lattice constant. This agrees well with data from Dubiel and Zinn [55,56], which has shown that the linear decrease of the isomer shift of $Fe_{1-x}V_x$ with the V concentration is dominated by the direct transfer of s-electrons from V to Fe. For the SRO samples within the shaded area between $x = 0.4$ and 0.5, a drastic reduction of the isomer shift compared to the *bcc* phase is evident. Moreover,

the isomer shifts are even smaller compared to the σ phase at the same concentration [31,35]. To understand such pronounced negative isomer shift, it is essential to understand the origin of the SRO phase. In our previous works with magnetron sputtered samples [12–14], it appeared at $x = 0.4$ both at 300 K and at elevated temperatures of 573 K, with a higher degree of SRO at the elevated growth temperatures. By using the MBE growth at variable growth temperatures, it is possible to clearly distinguish between the SRO phase at high growth temperatures and the *bcc*-phase at low growth temperatures, with a sharp transition in between. This allows for the conclusion, that the SRO phase is a structurally frustrated phase originating from incomplete chemical and structural ordering during σ-phase formation. How such short-range order can be characterized and compared to the equilibrium phases is still ongoing research, but based on the obtained results, the following conclusions can be made. The short-range ordered phase is almost amorphous in nature, as can be seen from the very broad, almost non-visible Bragg reflections in the XRD, showcasing strong structural disorder in comparison to the equilibrium phases. Further it shows strongly reduced ferromagnetism, as both the saturation magnetization and the hyperfine fields vanish. Ultimately, the isomer shift shows a very prominent fingerprint with its pronounced shift to large negative values for the short-range ordered samples. Already in the *bcc*-phase, the isomer shift directly depends on the V concentration, showing increasing negative shifts at increasing V concentrations [55, 56]. A similar observation was made for the σ-phase, where the isomer shift is directly dependent on the number of V nearest-neighbors, also with large negative shifts observed for sites with a high number of V nearest-neighbors and low open volume around that particular site [32,35]. This reveals, that structural change is accompanied by chemical ordering, increasing the probability of having unlike atoms as nearest-neighbors and by reducing/increasing the open volume around Fe/V atoms respectively, which would be in line with the observations made in [12], where different local environments were observed for Fe and V atoms. The negative isomer shift of the SRO samples even surpasses the one of the σ phase. Interestingly, this is not seen for the high x alloys, which also show only very broad Bragg reflections in the XRD. This implies that for the intermediate compositions, not only structural disorder in the form of mean square displacements of atoms or grain boundaries is essential to describing the disordered system, but an increase in chemical ordering and/or an increase of the Fe coordination number at the expense of V coordination, along with the volume decrease/increase around Fe/V are the main drivers behind the SRO. Furthermore, this makes the isomer shift a reliable probe for the chemical ordering tendencies in the intermediate alloy composition regime. These chemical ordering tendencies can be further understood by analyzing the Fe-partial VDOS of the SRO and *bcc* samples. Upon forming the SRO state, an overall broadening occurs and the low energy modes experience a softening, resulting in an overall increase of the (Fe-partial) vibrational entropy by a larger amount compared to the A2-B2 ordering transition [16]. Furthermore, the softening can be assumed as an indicator of the chemical ordering specific to the FeV system, if compared to the nanocrystalline-*bcc* system [43], which shows the broadening of the VDOS caused by the structural disorder but not a significant softening. Although the numbers presented above only account for the Fe atoms, the effects for V are expected to be even more pronounced, considering results for the element resolved VDOS [16] and EXAFS [12]. Another interesting parallel of the SRO films compared to the nanocrystalline films is the large slope in the low-energy region of the VDOS that could be due to a higher sound velocity or an increase of elastic discontinuities but, either way might be a fingerprint of the structural disorder of the system, leaving the nuclear inelastic scattering as a powerful tool for further studies of both structural and chemical disorder caused by the ion- or laser-induced selective phase transformation.

5. Conclusion

Thin-films of $Fe_{1-x}V_x$ were grown in the whole concentration range and at different substrate temperatures. For most of the sample compositions, the thin-films grow in the *bcc*-phase, showing the known properties such as deviation from Vegard's rule, a linear relationship between isomer shift and concentration, and antiparralel alignment of Fe and V moments. Beyond that, the SRO phase was found around equiatomic composition and only at elevated growth temperatures, which implies that it is a pre-stage of the σ-phase. The SRO phase is recognizable not only by the absence of narrow Bragg reflections in the XRD pattern and the absence of ferromagnetic order, but also by a very pronounced negative isomer shift, indicating a substantial increase of the electron density at the Fe nuclei, which is indicative of both reduction of the free volume around Fe and the increase of V- nearest neighbors. Furthermore, the Fe-partial VDOS shows not only broadening, as expected from the structural disorder, but also softening of the transversal modes that results in the overall increase of the vibrational entropy within the SRO-phase, both stabilizing the SRO phase and indicating chemical ordering. In conclusion, the structural disordering of the SRO Fe–V alloy is accompanied by chemical ordering, effectively increasing the probability of finding unlike nearest-neighbors. Especially the isomer shift and nuclear inelastic scattering have proven to show pronounced and reliable fingerprints of structural and chemical disorder, opening up possibilities to investigate their correlations with, e.g. the presence of vacancies, grain boundaries or other structural defects.

CRediT authorship contribution statement

Simon Rauls: Writing – original draft, Visualization, Investigation, Formal analysis, Conceptualization. **Benedikt Eggert:** Writing – review & editing, Conceptualization. **Shadab Md. Anwar:** Writing – review & editing. **Tobias Lojewski:** Writing – review & editing, Investigation. **Tom Helbig:** Writing – review & editing, Investigation. **Aleksandr Chumakov:** Writing – review & editing, Investigation. **Dimitrios Bessas:** Writing – review & editing, Investigation. **Radu Abrudan:** Writing – review & editing, Investigation. **Katharina Ollefs:** Writing – review & editing. **Kay Potzger:** Writing – review & editing. **Jürgen Fassbender:** Writing – review & editing. **Rantej Bali:** Writing – review & editing, Project administration, Funding acquisition, Conceptualization. **Heiko Wende:** Writing – review & editing, Supervision, Resources, Project administration, Funding acquisition, Conceptualization.

Declaration of competing interest

The authors declare that they have no known competing financial interests or personal relationships that could have appeared to influence the work reported in this paper.

Acknowledgments

We gratefully acknowledge funding by the German Research Foundation (DFG) through project No. 322462997 (BA 5656/1-2|WE 2623/14-2). We thank the European Synchrotron Radiation Facility (ESRF) for provision of synchrotron radiation facilities under proposal number HC-5144, HC-5324 and Mr. J.P. Celse for his technical assistance during the beamtime. XMCD measurements were carried out at the PM3 beamline using the ALICE instrument installed (project number 231-12096ST) at the BESSY II electron storage ring, operated by the Helmholtz-Zentrum Berlin für Materialien und Energie and we acknowledge the admission of beamtime. The authors also thank F. Radu, L. Gurin and J. Salgado Cabaço for their support during the beamtime. At last, we thank U. von Hörsten for his valuable technical assistance.

Appendix A. Supplementary data

Supplementary material related to this article can be found online at https://doi.org/10.1016/j.jallcom.2025.183282.

References

[1] J. Ehrler, M. He, M.V. Shugaev, N.I. Polushkin, S. Wintz, V. Liersch, S. Cornelius, R. Hübner, K. Potzger, J. Lindner, J. Fassbender, A.A. Ünal, S. Valencia, F. Kronast, L.V. Zhigilei, R. Bali, Laser-Rewriteable Ferromagnetism at Thin-Film Surfaces, ACS Appl. Mater. Interfaces 10 (17) (2018) 15232–15239, http://dx.doi.org/10.1021/acsami.8b01190.

[2] A.A. Ünal, A. Parabas, A. Arora, J. Ehrler, C. Barton, S. Valencia, R. Bali, T. Thomson, F. Yildiz, F. Kronast, Laser-driven formation of transient local ferromagnetism in FeRh thin films, LEEM/PEEM-10, Ultramicroscopy 183 (2017) 104–108, http://dx.doi.org/10.1016/j.ultramic.2017.03.024.

[3] R. Bali, S. Wintz, F. Meutzner, R. Hübner, R. Boucher, A.A. Ünal, S. Valencia, A. Neudert, K. Potzger, J. Bauch, F. Kronast, S. Facsko, J. Lindner, J. Fassbender, Printing Nearly-Discrete Magnetic Patterns Using Chemical Disorder Induced Ferromagnetism, Nano Lett. 14 (2) (2014) 435–441, http://dx.doi.org/10.1021/nl404521c.

[4] D.G. Merkel, A. Lengyel, D.L. Nagy, A. Németh, Z.E. Horváth, C. Bogdán, M.A. Gracheva, G. Hegedűs, S. Sajti, G.Z. Radnóczi, E. Szilágyi, Reversible control of magnetism in FeRh thin films, Sci. Rep. 10 (1) (2020) 13923, http://dx.doi.org/10.1038/s41598-020-70899-x.

[5] W. Griggs, B. Eggert, M.O. Liedke, M. Butterling, A. Wagner, U. Kentsch, E. Hirschmann, M. Grimes, A.J. Caruana, C. Kinane, H. Wende, R. Bali, T. Thomson, Depth selective magnetic phase coexistence in FeRh thin films, APL Mater. 8 (12) (2020) 121103, http://dx.doi.org/10.1063/5.0032130.

[6] S.P. Bennett, A. Herklotz, C.D. Cress, A. Ievlev, C.M. Rouleau, I.I. Mazin, V. Lauter, Magnetic order multilayering in FeRh thin films by He-Ion irradiation, Mater. Res. Lett. 6 (1) (2018) 106–112, http://dx.doi.org/10.1080/21663831.2017.1402098.

[7] E. La Torre, A. Smekhova, C. Schmitz-Antoniak, K. Ollefs, B. Eggert, B. Cöster, D. Walecki, F. Wilhelm, A. Rogalev, J. Lindner, R. Bali, R. Banerjee, B. Sanyal, H. Wende, Local probe of irradiation-induced structural changes and orbital magnetism in $Fe_{60}Al_{40}$ thin films via an order-disorder phase transition, Phys. Rev. B 98 (2) (2018) 024101, http://dx.doi.org/10.1103/PhysRevB.98.024101.

[8] D.G. Merkel, G. Hegedűs, M. Gracheva, A. Deák, L. Illés, A. Németh, F. Maccari, I. Radulov, M. Major, A.I. Chumakov, D. Bessas, D.L. Nagy, Z. Zolnai, S. Graning, K. Sájerman, E. Szilágyi, A. Lengyel, A Three-Dimensional Analysis of Magnetic Nanopattern Formation in FeRh Thin Films on MgO Substrates: Implications for Spintronic Devices, ACS Appl. Nano Mater. 5 (4) (2022) 5516–5526, http://dx.doi.org/10.1021/acsanm.2c00511.

[9] S. Sorokin, M.S. Anwar, G. Hlawacek, R. Boucher, J. Salgado-Cabaco, K. Potzger, J. Lindner, J. Faßbender, R. Bali, Transport properties of $Fe_{60}Al_{40}$ during the B2 to A2 structural phase transition, New J. Phys. 25 (9) (2023) 093036, http://dx.doi.org/10.1088/1367-2630/acdf13.

[10] M. Andreeva, A. Smekhova, R. Baulin, Y. Repchenko, R. Bali, C. Schmitz-Antoniak, H. Wende, I. Sergueev, K. Schlage, H.-C. Wille, Evolution of the magnetic hyperfine field profiles in an ion-irradiated $Fe_{60}Al_{40}$ film measured by nuclear resonant reflectivity, J. Synchrotron Radiat. 28 (5) (2021) 1535–1543, http://dx.doi.org/10.1107/S1600577521007694.

[11] B. Eggert, A. Schmeink, J. Lill, M. Oskar Liedke, U. Kentsch, M. Butterling, A. Wagner, S. Pascarelli, K. Potzger, J. Lindner, T. Thomson, J. Fassbender, K. Ollefs, W. Keune, R. Bali, H. Wende, Magnetic response of FeRh to static and dynamic disorder, RSC Adv. 10 (24) (2020) 14386–14395, http://dx.doi.org/10.1039/D0RA01410A.

[12] S. Rauls, M.S. Anwar, M.O. Liedke, M. Butterling, B. Eggert, E. Welter, D. Günzing, P. Klaßen, A. Herman, O. Hellwig, J. Fassbender, J. Lindner, A. Wagner, K. Potzger, R. Bali, H. Wende, Evolution of defects and local environment during the magnetostructural phase transformation in $Fe_{60}Al_{40}$ thin films, Phys. Rev. Mater. 8 (11) (2024) 114415, http://dx.doi.org/10.1103/PhysRevMaterials.8.114415.

[13] T. Pflug, J. Pablo-Navarro, M.S. Anwar, M. Olbrich, C. Magén, M.R. Ibarra, K. Potzger, J. Faßbender, J. Lindner, A. Horn, R. Bali, Laser-Induced Positional and Chemical Lattice Reordering Generating Ferromagnetism, Adv. Funct. Mater. 34 (13) (2024) 2311951, http://dx.doi.org/10.1002/adfm.202311951.

[14] M.S. Anwar, H. Cansever, B. Boehm, R.A. Gallardo, R. Hübner, S. Zhou, U. Kentsch, S. Rauls, B. Eggert, H. Wende, K. Potzger, J. Fassbender, K. Lenz, J. Lindner, O. Hellwig, R. Bali, Depth-Adjustable Magnetostructural Phase Transition in Fe60V40 Thin Films, ACS Appl. Electron. Mater. 4 (8) (2022) 3860–3869, http://dx.doi.org/10.1021/acsaelm.2c00499.

[15] C. Diaz-Caraveo, B.K. C, J.A.M. San Martín, Lattice dynamics and free energies of Fe–V alloys with thermal and chemical disorder, J. Phys.: Condens. Matter. 36 (44) (2024) 445401, http://dx.doi.org/10.1088/1361-648X/ad66a5.

[16] J.A. Muñoz, M.S. Lucas, O. Delaire, M.L. Winterrose, L. Mauger, C.W. Li, A.O. Sheets, M.B. Stone, D.L. Abernathy, Y. Xiao, P. Chow, B. Fultz, Positive Vibrational Entropy of Chemical Ordering in FeV, Phys. Rev. Lett. 107 (11) (2011) 115501, http://dx.doi.org/10.1103/PhysRevLett.107.115501.

[17] J.M. Sanchez, M.C. Cadeville, V. Pierron-Bohnes, G. Inden, Experimental and theoretical determination of the metastable Fe-V phase diagram, Phys. Rev. B 54 (13) (1996) 8958–8961, http://dx.doi.org/10.1103/PhysRevB.54.8958.

[18] C. Vouille, A. Barthélémy, F. Elokan Mpondo, A. Fert, P.A. Schroeder, S.Y. Hsu, A. Reilly, R. Loloee, Microscopic mechanisms of giant magnetoresistance, Phys. Rev. B 60 (9) (1999) 6710–6722, http://dx.doi.org/10.1103/physrevb.60.6710.

[19] H. Wende, A. Scherz, F. Wilhelm, K. Baberschke, Induced magnetism at thin-film interfaces probed by means of x-ray magnetic circular dichroism, J. Phys.: Condens. Matter. 15 (5) (2003) S547–S559, http://dx.doi.org/10.1088/0953-8984/15/5/309.

[20] A. Scherz, P. Poulopoulos, R. Nünthel, J. Lindner, H. Wende, F. Wilhelm, K. Baberschke, Direct probe of interdiffusion effects on the induced V spin polarization at Fe/V interfaces, Phys. Rev. B 68 (14) (2003) 140401, http://dx.doi.org/10.1103/PhysRevB.68.140401.

[21] M.V. Nevitt, A.T. Aldred, Ferromagnetism in V-Fe and Cr-Fe Alloys, J. Appl. Phys. 34 (3) (1963) 463–468, http://dx.doi.org/10.1063/1.1729295.

[22] J.C. Krause, J. Schaf, M.I. da Costa, C. Paduani, Effect of composition and short-range order on the magnetic moments of $Fe_{1-x}V_x$ alloys, Phys. Rev. B 61 (9) (2000) 6196–6204, http://dx.doi.org/10.1103/PhysRevB.61.6196.

[23] M. Arora, E.K. Delczeg-Czirjak, G. Riley, T. Silva, H.T. Nembach, O. Eriksson, J.M. Shaw, Magnetic Damping in Polycrystalline Thin-Film Fe – V Alloys, Phys. Rev. Appl. 15 (5) (2021) 054031, http://dx.doi.org/10.1103/PhysRevApplied.15.054031.

[24] M. Bersweiler, K. Watanabe, H. Sato, F. Matsukura, H. Ohno, Magnetic properties of FeV/MgO-based structures, Appl. Phys. Express 10 (8) (2017) 083001, http://dx.doi.org/10.7567/APEX.10.083001.

[25] T. Devolder, T. Tahmasebi, S. Eimer, T. Hauet, S. Andrieu, Compositional dependence of the magnetic properties of epitaxial FeV/MgO thin films, Appl. Phys. Lett. 103 (24) (2013) 242410, http://dx.doi.org/10.1063/1.4845375.

[26] D.A. Smith, S. Takei, B. Brann, L. Compton, F. Ramos-Diaz, M.J. Simmers, S. Emori, Diffusive and Fluidlike Motion of Homochiral Domain Walls in Easy-Plane Magnetic Strips, Phys. Rev. Appl. 16 (5) (2021) 054002, http://dx.doi.org/10.1103/PhysRevApplied.16.054002.

[27] D.A. Smith, A. Rai, Y. Lim, T.Q. Hartnett, A. Sapkota, A. Srivastava, C. Mewes, Z. Jiang, M. Clavel, M.K. Hudait, D.D. Viehland, J.J. Heremans, P.V. Balachandran, T. Mewes, S. Emori, Magnetic Damping in Epitaxial Iron Alloyed with Vanadium and Aluminum, Phys. Rev. Appl. 14 (3) (2020) 034042, http://dx.doi.org/10.1103/PhysRevApplied.14.034042.

[28] D. Ourdani, Y. Roussigné, S.M. Chérif, M.S. Gabor, M. Belmeguenai, Thickness dependence of magnetic properties of Ir/FeV-based systems, Phys. Rev. Mater. 7 (3) (2023) 034408, http://dx.doi.org/10.1103/PhysRevMaterials.7.034408.

[29] J. Cieslak, J. Tobola, S.M. Dubiel, Theoretical study of magnetic properties and hyperfine interactions in σ-FeV alloys, Intermetallics 22 (2012) 7–12, http://dx.doi.org/10.1016/j.intermet.2011.10.015.

[30] N. Kataoka, K. Sumiyama, Y. Nakamura, Metastable Crystalline and Amorphous Fe–V Alloys Produced by Vapor Quenching, Trans. Japan Inst. Met. 27 (11) (1986) 823–829, http://dx.doi.org/10.2320/matertrans1960.27.823.

[31] J. Cieslak, J. Tobola, S.M. Dubiel, Electronic structure of the σ phase of paramagnetic Fe-V alloys, Phys. Rev. B 81 (17) (2010) 174203, http://dx.doi.org/10.1103/PhysRevB.81.174203.

[32] J. Cieslak, J. Tobola, S.M. Dubiel, Electronic structure of the σ phase of paramagnetic Fe-V alloys, Phys. Rev. B 81 (17) (2010) 174203, http://dx.doi.org/10.1103/PhysRevB.81.174203.

[33] J. Cieślak, M. Reissner, S.M. Dubiel, J. Wernisch, W. Steiner, Influence of composition and annealing conditions on the site-occupation in the σ-phase of Fe–Cr and Fe–V systems, J. Alloys Compd. 460 (1) (2008) 20–25, http://dx.doi.org/10.1016/j.jallcom.2007.05.098.

[34] J. Cieślak, B.F.O. Costa, S.M. Dubiel, G. Le Caër, Kinetics of the sigma-to-alpha phase transformation caused by ball milling in near equiatomic Fe−Cr alloys, Phys. Rev. B 73 (18) (2006) 184123, http://dx.doi.org/10.1103/PhysRevB.73.184123.

[35] S.M. Dubiel, J. Cieślak, Sigma-Phase in Fe-Cr and Fe-V Alloy Systems and its Physical Properties, Crit. Rev. Solid State Mater. Sci. 36 (4) (2011) 191–208, http://dx.doi.org/10.1080/10408436.2011.589232.

[36] B. Fultz, G. Le Caür, P. Matteazzi, Mechanical alloying of Fe and V powders: Intermixing and amorphous phase formation, J. Mater. Res. 4 (6) (1989) 1450–1455, http://dx.doi.org/10.1557/JMR.1989.1450.

[37] U. von Hörsten, Pi program package, a Windows program for the evaluation of Mössbauer spectra. Download at, 2025, https://udue.de/Pi.

[38] T. Kachel, The PM3 beamline at BESSY II, J. Large-Scale Res. Facil. JLSRF 2 (2016) http://dx.doi.org/10.17815/jlsrf-2-73, A48–A48.

[39] A.I. Chumakov, A.Q.R. Baron, R. Rüffer, H. Grünsteudel, H.F. Grünsteudel, A. Meyer, Nuclear Resonance Energy Analysis of Inelastic X-Ray Scattering, Phys. Rev. Lett. 76 (22) (1996) 4258–4261, http://dx.doi.org/10.1103/PhysRevLett.76.4258.

[40] J.F. Smith, The Fe-V (Iron-Vanadium) system, Bull. Alloy. Phase Diagrams 5 (2) (1984) 184–194, http://dx.doi.org/10.1007/BF02868958.

[41] R. Hanneman, A. Mariano, Placeholder, Trans. the AIME 230 (1964) 937–939.

[42] A. Scherz, H. Wende, K. Baberschke, Fine structure of X-ray magnetic circular dichroism for early 3d transition metals, Appl. Phys. A 78 (6) (2004) 843–846, http://dx.doi.org/10.1007/s00339-003-2440-x.

[43] B. Fultz, J.L. Robertson, T.A. Stephens, L.J. Nagel, S. Spooner, Phonon density of states of nanocrystalline Fe prepared by high-energy ball milling, J. Appl. Phys. 79 (11) (1996) 8318–8322, http://dx.doi.org/10.1063/1.362543.

[44] O.N. Miroshkina, B. Eggert, J. Lill, B. Beckmann, D. Koch, M.Y. Hu, T. Lojewski, S. Rauls, F. Scheibel, A. Taubel, M. Šob, K. Ollefs, O. Gutfleisch, H. Wende, M.E. Gruner, M. Friák, Impact of magnetic and antisite disorder on the vibrational densities of states in Ni 2 MnSn Heusler alloys, Phys. Rev. B 106 (21) (2022) 214302, http://dx.doi.org/10.1103/PhysRevB.106.214302.

[45] W. Keune, T. Ruckert, B. Sahoo, W. Sturhahn, T.S. Toellner, E.E. Alp, R. Röhlsberger, Atomic vibrational density of states in crystalline and amorphous Tb_1-xFe_x alloy thin films studied by nuclear resonant inelastic X-Ray scattering (NRIXS), J. Phys.: Condens. Matter. 16 (5) (2004) S379, http://dx.doi.org/10.1088/0953-8984/16/5/004.

[46] A.I. Chumakov, G. Monaco, A. Fontana, A. Bosak, R.P. Hermann, D. Bessas, B. Wehinger, W.A. Crichton, M. Krisch, R. Rüffer, G. Baldi, G. Carini Jr., G. Carini, G. D'Angelo, E. Gilioli, G. Tripodo, M. Zanatta, B. Winkler, V. Milman, K. Refson, M.T. Dove, N. Dubrovinskaia, L. Dubrovinsky, R. Keding, Y.Z. Yue, Role of Disorder in the Thermodynamics and Atomic Dynamics of Glasses, Phys. Rev. Lett. 112 (2) (2014) 025502, http://dx.doi.org/10.1103/PhysRevLett.112.025502.

[47] S. Stankov, M. Miglierini, A.I. Chumakov, I. Sergueev, Y.Z. Yue, B. Sepiol, P. Svec, L. Hu, R. Rüffer, Vibrational thermodynamics of $Fe_{90}Zr_7B_3$ nanocrystalline alloy from nuclear inelastic scattering, Phys. Rev. B 82 (14) (2010) 144301, http://dx.doi.org/10.1103/PhysRevB.82.144301.

[48] I. Mirebeau, G. Parette, J.W. Cable, Polarised neutron study of iron-vanadium alloys, J. Phys. F: Met. Phys. 17 (1) (1987) 191–198, http://dx.doi.org/10.1088/0305-4608/17/1/024.

[49] A. Scherz, H. Wende, K. Baberschke, J. Minár, D. Benea, H. Ebert, Relation between L2,3 XMCD and the magnetic ground-state properties for the early 3d element V, Phys. Rev. B 66 (18) (2002) 184401, http://dx.doi.org/10.1103/PhysRevB.66.184401.

[50] Y. Guan, C. Scheck, W.E. Bailey, Element-specific spin and orbital moments in $Fe_{1-x}V_x$ alloys, Current Perspectives: Spintronics, J. Magn. Magn. Mater. 321 (8) (2009) 1039–1044, http://dx.doi.org/10.1016/j.jmmm.2008.10.014.

[51] E. Goering *, X-ray magnetic circular dichroism sum rule correction for the light transition metals, Phil. Mag. 85 (25) (2005) 2895–2911, http://dx.doi.org/10.1080/14786430500155221, Publisher: Taylor & Francis _eprint.

[52] A. Scherz, H. Wende, C. Sorg, K. Baberschke, J. Minr, D. Benea, H. Ebert, Limitations of integral XMCD sum-rules for the early 3d elements, Phys. Scr. 2005 (T115) (2005) 586, http://dx.doi.org/10.1238/Physica.Topical.115a00586, URL https://iopscience.iop.org/article/10.1238/Physica.Topical.115a00586/meta. Publisher: IOP Publishing.

[53] G.K. Wertheim, V. Jaccarino, J.H. Wernick, D.N.E. Buchanan, Range of the Exchange Interaction in Iron Alloys, Phys. Rev. Lett. 12 (1) (1964) 24–27, http://dx.doi.org/10.1103/PhysRevLett.12.24.

[54] I. Vincze, I.A. Campbell, Mossbauer measurements in iron based alloys with transition metals, J. Phys. F: Met. Phys. 3 (3) (1973) 647–663, http://dx.doi.org/10.1088/0305-4608/3/3/023.

[55] S.M. Dubiel, W. Zinn, Further comparison of model predictions with measured Fe-site spin- and charge-density changes in various bcc Fe-based alloys, Phys. Rev. B 29 (4) (1984) 2279–2282, http://dx.doi.org/10.1103/PhysRevB.29.2279.

[56] S.M. Dubiel, W. Zinn, Application of the Mössbauer effect in the investigation of the substitution induced spin and charge density changes in bcc-iron, J. Magn. Magn. Mater. 45 (2) (1984) 298–304, http://dx.doi.org/10.1016/0304-8853(84)90022-2.